Applied Catalysis B: Environmental 314 (2022) 121515

Contents lists available at ScienceDirect

Applied Catalysis B: Environmental

journal homepage: www.elsevier.com/locate/apcatb

Synergetic effect of Cu^0 −Cu^+ derived from layered double hydroxides toward catalytic transfer hydrogenation reaction

Yingyu Ren, Yusen Yang *, Lifang Chen, Lei Wang, Yawen Shi, Pan Yin, Wenlong Wang, Mingfei Shao, Xin Zhang, Min Wei *

State Key Laboratory of Chemical Resource Engineering, Beijing Advanced Innovation Center for Soft Matter Science and Engineering, Beijing University of Chemical Technology, Beijing 100029, PR China

ARTICLE INFO

Keywords:
Layered double hydroxides
Dual active sites
Catalytic transfer hydrogenation
Active hydrogen species
Synergetic catalysis

ABSTRACT

As a safe and environmentally friendly selective hydrogenation method, catalytic transfer hydrogenation (CTH) has aroused great interest in preparation of high-value-added products from biomass derived resources. Herein, a Cu-based catalyst (Cu/CuAl-MMO-400) was prepared by structural topological transformation of layered double hydroxides (LDHs) precursor, which displayed promising catalytic behavior toward CTH reaction of furfural (FAL) with 2-propanol (2-POL) as the hydrogen donor. Notably, the reaction rate is as high as 0.125 mol g^{-1} h^{-1}, which is superior to previously reported non-noble metal catalysts. A combination investigation based on XPS, XANES and Bader charge confirms the co-existence of Cu^0 and Cu^+ sites on the surface of Cu nanoparticles. Both experimental studies (*in situ* DRIFTS and isotope labelling MS) and DFT calculations reveal that the Cu^0—Cu^+ synergistic effect plays a vital role in determining catalytic behavior: the Cu^+ species acts as both dehydrogenation and hydrogenation active site; while the Cu^0 site promotes the transfer of H atoms between adsorbed substrates. This work substantiates a Cu^0 −Cu^+ synergetic catalysis by establishing structure-property correlation and revealing reaction pathway, which could be extended to other CTH reactions in the upgrading processes of biomass.

1. Introduction

With rapid depletion of fossil fuel and enormous issue of increasing environment pollution, renewable biomass resources as an effective alternative to offer a mass of high-energy density fuels and valuable functionalized chemicals have evoked widespread attention [1–3]. The reaction of selective hydrogenation is of significance for obtaining high value-added products in upgrading process of biomass resources, due to the coexistence of various unsaturated functional groups in biomass feed-stocks (*e.g.*, furfural) [4–8]. Generally, two conventional techniques have been effectually used in the selective hydrogenation reactions [9–11]. The first one is the use of molecular hydrogen (H_2) as the hydrogen donor, providing an excellent hydrogenation efficiency [12,13]. Although much progress has been made in direct hydrogenation route, the storage, transportation and processing of H_2 are difficult and costly in remote areas where biomass resources abound [14,15]. The second technique, catalytic transfer hydrogenation (CTH) in which hydrogen-containing organics (especially cheap and abundant alcohol compounds) serving as a hydrogen donor, avoids the employment of H_2, thus greatly reducing the complicacy and expense of experimental equipment, and obtain additional dehydrogenation products [16–22].

Despite the great efforts devoted to CTH reactions [23,24], several issues still remain unresolved about the reasonable design and accurate synthesis of heterogeneous catalysts to achieve low-energy and more economical processes. A variety of experimental schemes for preparation of efficient catalysts by regulating the structure, morphology and surface property have been developed, in which Cu-based catalysts have shown promising catalytic performance (*e.g.*, Cu/CaAlO, Cu/AC-SO_3H, and Cu/Cu_2O-MC) [25–28]. However, the control over geometric and electronic structure of Cu-based catalyst is rather difficult, owing to a facile aggregation of Cu nanoparticles with complicated valence states [29,30]. This would impose an unexpectable influence on their catalytic performance [31,32]. Moreover, the active sites toward dehydrogenation of hydrogen donors and hydrogenation of hydrogen acceptors, as well as the transfer route of active hydrogen species between the two substrates still remain ambiguous. A detailed and systematic study on

* Corresponding authors.
E-mail addresses: yangyusen@mail.buct.edu.cn (Y. Yang), weimin@mail.buct.edu.cn (M. Wei).

https://doi.org/10.1016/j.apcatb.2022.121515
Received 18 January 2022; Received in revised form 7 May 2022; Accepted 11 May 2022
Available online 15 May 2022

the synergetic catalysis of active sites and reaction mechanism of CTH is highly imperative for the design and preparation of fresh catalysts with greatly enhanced catalytic behavior [33].

Inspired by the above viewpoints, we prepared Cu-based nano-catalysts supported on CuAl-mixed metal oxide (CuAl-MMO) based on a structural topotactic transformation process of Cu_2Al-layered double hydroxides (Cu_2Al-LDHs) (Fig. 1a). By means of an *in situ* reduction treatment of Cu_2Al-LDHs at different temperatures, Cu nanoparticles embedded in CuAl-MMO substrate with a highly-uniform dispersion were obtained (denoted as Cu/CuAl-MMO-*T*, *T* = 300, 400, 500 and 600 °C). A systematic investigation including HR-TEM, XPS and *in situ* EXAFS verifies that the Cu^0/Cu^+ molar ratio increases gradually with the rise of reduction temperature from 300 to 600 °C. The catalytic performance in the CTH reaction (Fig. S1) of furfural (FAL) with 2-propanol (2-POL) as the hydrogen donor was evaluated over Cu/CuAl-MMO-*T*. The reaction rate of the optimal sample reaches up to 0.125 mol g^{-1} h^{-1}, which is 3 − 10 times superior that of non-noble metal catalysts ever reported; and a satisfactory stability is demonstrated within five catalytic cycles. Investigations on the structure-property correlation based on *in situ* FT-IR, isotopic labelling MS and theoretical calculations confirm that the CTH reaction of FAL occurs through a metal hydride pathway with the assistance of Cu^0 −Cu^+ synergistic effect, in which both substrates (FAL and 2-POL) undergo activation adsorption at Cu^+ site whilst Cu^0 site promotes the transfer of H atoms on the catalyst surface. This work demonstrates a synergistic catalysis of dual active sites derived from LDHs precursors, which would pave a way in the design and synthesis of high-performance catalysts toward CTH reactions.

2. Experimental section

2.1. Materials

All the reagents ($Cu(NO_3)_2{\cdot}3H_2O$, $Al(NO_3)_3{\cdot}9H_2O$, NaOH, Na_2CO_3, FAL and 2-POL) were purchased from Aladdin. Throughout the experimental process, deionized water was used, and all reagents were used without further purification.

2.2. Catalyst synthesis

Synthesis of Cu_2Al-LDHs precursors: The Cu_2Al-LDHs precursor was synthesized by a coprecipitation method [34]. In a typical procedure, Cu $(NO_3)_2{\cdot}3H_2O$ (0.1 M) and $Al(NO_3)_3{\cdot}9H_2O$ (0.5 M) were dissolved in deionized water (200 mL) to obtain a solution (solution A), while NaOH (0.24 M) and Na_2CO_3 (0.1 M) were dissolved in another 200 mL of water to obtain an alkaline solution (solution B). Under vigorous stirring conditions, 10 mL of deionized water was used as the mother liquor, to which solution A and solution B were slowly added dropwise with the pH value keeping at 9.0. The obtained mixture was sealed in a Teflon autoclave, aging at 100 °C for 12 h. The resulting precipitate was separated, washed thoroughly with water and ethanol and then dried at 60 °C for 12 h.

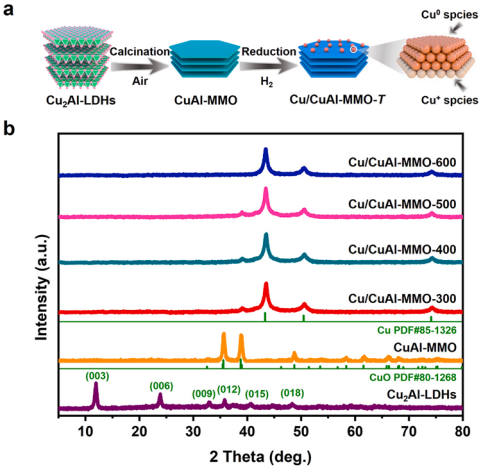

Fig. 1. (a) Schematic representation for the preparation of Cu/CuAl-MMO catalysts. (b) XRD patterns of Cu_2Al-LDHs, CuAl-MMO and the resulting Cu/CuAl-MMO samples: Cu/CuAl-MMO-300, Cu/CuAl-MMO-400, Cu/CuAl-MMO-500 and Cu/CuAl-MMO-600, respectively.

Synthesis of Cu/CuAl-MMO-*T* catalysts: Typically, the above Cu_2Al-LDHs precursor was calcined in air at 500 °C for 4.0 h to obtain mixed metal oxide (denoted as CuAl-MMO). Subsequently, the obtained CuAl-MMO was reduced in a H_2/N_2 (1/9, v/v) flow at 300, 400, 500 and 600 °C for 4 h, respectively, and then slowly cooled to room temperature. Finally, the sample was stored and transferred in a nitrogen pack for further use.

2.3. Catalytic evaluation

CTH of FAL was evaluated by using a stainless-steel reactor of 50 mL. Briefly, FAL (0.6 g), 2-POL (18 mL) and catalyst (0.05 g) were added into the reactor. After replacing the internal air by charging with nitrogen gas (2.0 MPa) five times, nitrogen gas of 0.1 MPa was charged into the reactor as a protective gas for the reaction. Then the reactor temperature was heated to 200 °C to trigger the reaction with 700 rpm magnetic stirring. A gas chromatograph (GC-2014 C, Shimadzu Company) equipped with flame ionization detector (FID) was used to analyze the reaction products. The quantification was carried out using the external standard method. The hydrogen balance is calculated as the ratio between the molar amount of H consumed by the hydrogenation of substrate and the molar amount of H produced by the dehydrogenation of hydrogen donor:

$$\text{Hydrogen Balance}(\%) = \frac{n_{\text{FOL}} + 2n_{\text{MF}}}{n_{\text{acetone}}} \times 100\% \quad (1)$$

where n_{FOL}, n_{MF} and n_{acetone} represent the molar amount of the hydrogenation product FOL, MF and the dehydrogenation product acetone, respectively.

The turnover frequency (TOF, h^{-1}) is calculated as substrate consumption rate of FAL per surface Cu atom:

$$\text{TOF} = \frac{n_{\text{FAL}}}{m_{\text{cat}} \times (D_{Cu^0} + D_{Cu^+}) \times t} \times 100\% \quad (2)$$

$$D_{Cu^+} = \frac{D_{Cu^0}}{x_{Cu^0/Cu^+}} \quad (3)$$

where n_{FAL} is the molar amount of FAL converted; m_{cat} denotes the quality of catalyst; *t* is the reaction time; D_{Cu^0} (mmol g^{-1}) represents the surface Cu^0 concentration measured from N_2O titration; D_{Cu^+} (mmol g^{-1}) represents the surface Cu^+ concentration; x_{Cu^0/Cu^+} is the molar ratio of Cu^0/Cu^+ determined by XAES.

2.4. Characterization instrumentations

The X-ray diffraction (XRD) measurements were performed on a Rigaku XRD-6000 diffractometer by using Cu Kα radiation (λ = 0.15418 nm, 40 kV and 40 mA), with a scanning rate of 10 °C min^{-1} and a 2θ angle from 5° to 80°. Scanning electron microscope (SEM) performed on a Zeiss Supra 55, as well as Transmission electron microscopy (TEM) and high-resolution transmission electron microscopy (HR-TEM) performed on JEOL JEM-2010 were used to obtaining the microstructure morphology of the catalysts. The nitrogen adsorption-desorption isotherms were measured on a Micromeritics ASAP 2020 Instrument, and the specific surface area was determined by the Brunauer-Emmett-Teller (BET) method. X-ray photoelectron spectra

(XPS) and X-ray excited Auger electron spectra (XAES) were obtained by using an AXIS SUPRA X-ray photoelectron spectrometer (pressure: 2×10^{-9} Torr) with an Al Kα X-ray source ($h\nu = 1486.6$ eV). Chemical state and the corresponding surface element composition of samples were determined by XPS Peak 4.1 program. Cu XAFS measurement was performed at the beamline 1W1B of the Beijing Synchrotron Radiation Facility (BSRF), Institute of High Energy Physics (IHEP), Chinese Academy of Sciences (CAS).

Temperature-programmed reduction (TPR) and temperature programmed desorption (TPD) were carried out on a Micromeritics AutoChem II 2920 equipped with a thermal conductivity detector (TCD). In a typical process of the H_2-TPR program, the sample (100 mg) sealed in a quartz tube reactor was pretreated in Ar flow, and then raised to 900 °C with a heating rate of 10 °C min^{-1} in a flow of H_2/Ar (1:9, v/v). In the case of CO_2-TPD, the sample (100 mg) was first reduced at the respective temperature (from 300 to 600 °C) for 1 h in 10 vol% H_2/Ar, followed by flushing with Ar. When the temperature was cooled down to 50 °C, CO_2 was introduced until saturation and then Ar was purged to remove physically-adsorbed CO_2. Finally, the temperature was raised to 600 °C with a rate of 10 °C min^{-1} to release the adsorbed CO_2. To measure the exposed metallic Cu, the N_2O oxidation and H_2 reduction method (N_2O titration) were performed at a Micromeritics AutoChem II 2920. Briefly, the sample was pretreatment in a H_2/He (1/9, v/v) flow at the respective temperature (from 300 to 600 °C) for 1 h and cooled to 25 °C, followed by flushing with He for 0.5 h. Then N_2O was introduced as an oxidant for 2 h to ensure that all surface Cu^0 species was oxidized to Cu^+. Finally, after He was purged to remove physisorbed N_2O, the Cu_2O from the previous oxidation was reduced to metallic Cu in a H_2/He (1/9, v/v) stream at corresponding temperature (from 300 to 600 °C) for 3 h. The amount of the surface metallic Cu species on the catalyst can be calculated.

The isotopic labeling measurement was performed by a Gas chromatography-mass spectrometry (GC-MS, Thermo Fisher ISQ Trace1300) equipped with a TR-WAXMS capillary column. In the experiment process of the labeled 2-POL-d_8, the reaction solution was replaced by 2-POL-d_8 (2 mL) plus *t*-butyl alcohol (16 mL) instead of the original 18 mL of 2-POL-d_0. FT-IR measurements of pyridine adsorption as well as substrate adsorption (FAL, 2-POL, a mixed substrate of FAL and 2-POL) were performed on Bruker infrared spectrometer (Transmission cell) equipped with a VERTEX-70 spectrometer. The sample (30 mg) was pressed into a self-supporting wafer, loaded in the Transmission cell, and then pretreated in a H_2/He (1/9, v/v) stream at corresponding temperature (from 300 to 600 °C) for 1 h. Typically, after cooling to 25 °C and purging He for 30 min, the background was collected at a resolution of 4 cm^{-1}. In the case of pyridine measurement, pyridine was introduced through vacuuming until saturation. The spectrum was collected after introducing He to remove the physically-adsorbed species. For the *in situ* FT-IR measurements of substrate adsorption, after pretreatment and background deduction, the substrate was pumped into the *in situ* reactor with 50 mL min^{-1} He flow for 15 min at 25, 50, 100, 150 and 200 °C respectively; subsequently, the physically-adsorbed species was removed by He flowing, followed by IR signal collection.

2.5. DFT calculations

Spin-polarized periodic DFT calculations were performed by the Vienna *ab initio* simulation package (VASP) [35]. The projector augmented wave (PAW) was used to describe electron-ion interactions [36]. The Perdew Burke Ernzerhof (PBE) functional was employed to calculate electron exchange and correlation energies, and the Grimme's DFT-D3 method was added to study the effect of van der Waals interaction [37,38]. All DFT calculations were performed at a cut-off energy of 400 eV, and the Brillouin zone was sampled using a 3 × 3 × 1 k-point grid. The climbing image general nudged elastic band (CI-NEB) or the dimer method was performed to locate the transition states (TSs) [39,40].

In this work, according to the experimental XRD and HR-TEM results, computational models of the three samples (Al_2O_3, Cu and Cu/CuAl-MMO) are built for DFT calculations for the purpose of studying the microstructures (Fig. S2). The functional was selected by using XRD cell parameters as the benchmark for ensuring the reliability of the calculated models. The Cu-Al_2O_3 interfacial structure was constructed by adding a two-layer Cu strip on the top of stoichiometric Al_2O_3(110) surface. The Al_2O_3(110) slab was set as two layers in thickness with a *p* (2 ×2) periodic unit cell, and a vacuum space of 15 Å was added on the surface to avoid interactions between slabs. The Cu(111) plate was set as a four-layer *p*(4 ×4) periodic unit cell. The bottom layer of 15 Å was constrained to prevent the atoms from moving during the optimization calculations. As shown in Fig. S2, the calculated lattice constants (*b*) of Cu(111) and Al_2O_3(110) crystal are 10.22 and 10.25 Å, respectively. The calculated deviation between Cu(111) and Al_2O_3(110) surface is merely 0.29%; therefore, the extension of Cu in Cu/CuAl-MMO model would have insignificant influence on the adsorption behavior of intermediates. After the structure optimization, a stable structure of Cu/CuAl-MMO was obtained. Moreover, the adsorption energy of furfural was calculated on two-layer Cu_4, three-layer Cu_6 and three-layer Cu_8 strips, which showed the values of − 0.88 eV, − 0.98 eV and − 0.82 eV, respectively (Fig. S3). Such a small deviation (~0.1 eV) should not have a decisive effect on the main conclusions.

Adsorption occurred on the topmost layer of each slab, and geometry optimization calculations were performed to obtain the relaxed structures of adsorbates on the Cu/CuAl-MMO slabs. The adsorption energy of each adsorbate, E_{ads}, was calculated as follows:

$$E_{ads} = E_{slab+adsorbate} - E_{slab} - E_{gas\text{-}phase\ molecule} \quad (4)$$

where $E_{slab+adsorbate}$, E_{slab}, and $E_{gas\text{-}phase\ molecule}$ are the overall energy, clean slab energy, and the energy of free adsorbate in the gas phase, respectively.

The reaction energy barrier is calculated as.

$$E_b = E(TS) - E(IS) \quad (5)$$

where *E*(IS) and *E*(TS) are the energies of the initial state (IS) and transition state (TS), respectively.

All thermodynamic properties (Table S1) were calculated based on the molecular vibration analysis from the DFT calculations [41]. The Gibbs free energies were calculated at 200 °C as.

$$G = E_{DFT} + E_{ZPE} - TS \quad (6)$$

where E_{DFT}, E_{ZPE}, *T* and *S* are the DFT total energy, the zero-point vibrational energy (ZPE) obtained from the calculated vibrational frequencies, the reaction temperature (200 °C), and the entropy of the studied system, respectively.

3. Results and discussion

3.1. Characterizations on structure and morphology of Cu/CuAl-MMO samples

The Cu-based catalysts were prepared based on a structural topotactic transformation of Cu_2Al-LDHs. Firstly, the Cu_2Al-LDHs precursor was obtained *via* a coprecipitation method reported in our previous work [42], whose XRD pattern (Fig. 1b) is assigned to a characteristic structure of layered LDHs with (003) and (006) planes at 2θ 11.87° and 23.81°, respectively. The SEM images of Cu_2Al-LDHs (Fig. S4) display a flake-like morphology (diameter: 300–400 nm), showing a good crystallization. Subsequently, the LDHs precursor was calcined in air atmosphere to acquire a mixed metal oxide (CuAl-MMO), of which the reflections (Fig. 1b) at 35.56°, 38.76° and 48.74° are indexed to CuO phase (PDF#80–1268). Nevertheless, no characteristic feature of Al_2O_3 is discovered, demonstrating an amorphous phase. After a specific

reduction treatment in H_2 atmosphere (Fig. S5 and S6), the resulting Cu/CuAl-MMO-*T* samples (T = 300, 400, 500 and 600 °C) give the reflections located at 2θ 43.31°, 50.44° and 74.12°, which are designated as (111), (200) and (220) planes of metallic copper phase. No diffraction peak of Cu_2O phase is found in the XRD pattern, indicating a high dispersion of Cu^+ sites. In addition, the EPR spectrum (Fig. S7) of Cu/CuAl-MMO-400 does not show obvious signal attributed to oxygen vacancy (with g values of 2.003 and 1.960).

The SEM images (Fig. 2a1–d1) of all these Cu/CuAl-MMO samples show that they retain flake-like morphology of Cu_2Al-LDHs precursor, with highly dispersed nanoparticles anchored on the surface verified by TEM (Fig. 2a2–d2). The average size of Cu nanoparticles is 6.1, 6.7, 7.5 and 8.2 nm for Cu/CuAl-MMO-300, Cu/CuAl-MMO-400, Cu/CuAl-MMO-500 and Cu/CuAl-MMO-600, respectively, which accords well with the XRD results by Scherrer equation (Table 1). HR-TEM images (Fig. 2a3–d3) further reveal the clear lattice spacings (0.18 and 0.21 nm) according well with (200) and (111) planes of cubic Cu phase, respectively.

X-ray photoelectron spectroscopy (XPS) and X-ray-induced Auger electron spectroscopy (XAES) display electronic structure information on the surface of Cu/CuAl-MMO samples (Fig. 3a–b). As shown in Fig. 3a, Cu 2p spectra of the catalysts can be deconvoluted by Gaussian peak fitting way. The bands at 931.4 and 951.1 eV are ascribed to Cu $2p_{3/2}$ and Cu $2p_{1/2}$ of $Cu^{0/+}$; while the bands at 933.6 and 953.3 eV are attributed to Cu $2p_{3/2}$ and Cu $2p_{1/2}$ of Cu^{2+} with a satellite peak at 942.1 eV [43]. For these samples, a small amount of Cu^{2+} in the bulk phase have not been completely reduced. However, as the reduction temperature increased from 300 to 600 °C, the proportion of Cu^{2+} decreases significantly. Since Cu^0 and Cu^+ exhibit similar binding energies, Cu LMM Auger electron spectra (Fig. 3b) was used to distinguish the Cu species [44]. From the deconvolution results, the peaks at 914.9, 917.9, and 920.0 eV belong to Cu^+, Cu^{2+}, and Cu^0 species. The molar ratio of Cu^0/Cu^+ for these samples is calculated by integrating the Gaussian peak fitting of XAES (Table 1), which gives the following sequence: Cu/CuAl-MMO-300 (0.65) < Cu/CuAl-MMO-400 (0.85) < Cu/CuAl-MMO-500 (1.02) < Cu/CuAl-MMO-600 (1.18). In addition, Cu^0 surface concentration of these catalysts is measured according to classic N_2O titration (Table 1), which decreases from 1.15 to 1.12, to 0.83, and then to 0.72 mmol g^{-1} with the increase of reduction temperature from 300 to 600 °C. Based on the above-mentioned surface Cu^0/Cu^+ molar ratio and surface Cu^0 concentration, the surface Cu^+ concentration decreases from 1.77 to 1.32, to 0.81, and then to 0.61 mmol g^{-1}. With the increase of reduction temperature from 300 to 600 °C, the surface concentration of Cu^0 decreases gradually, owing to the increased Cu particle size with reduced dispersion degree of Cu. In addition, a higher reduction temperature causes a more sufficient reduction of copper species, resulting in the decrease in surface concentration of Cu^+ and Cu^{2+} species.

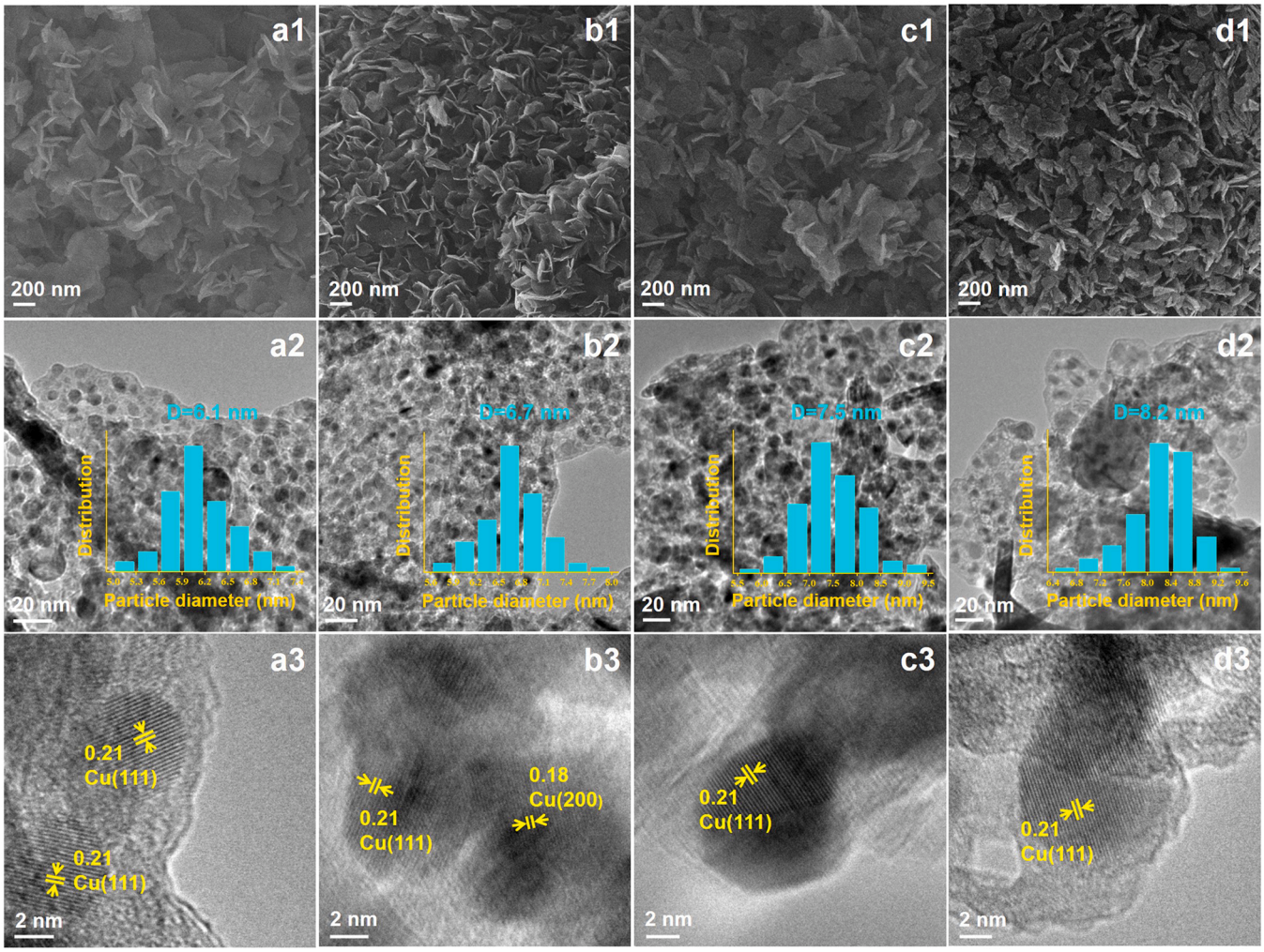

Fig. 2. SEM images of Cu/CuAl-MMO samples: (a1) Cu/CuAl-MMO-300, (b1) Cu/CuAl-MMO-400, (c1) Cu/CuAl-MMO-500 and (d1) Cu/CuAl-MMO-600. TEM images of Cu/CuAl-MMO samples: (a2) Cu/CuAl-MMO-300, (b2) Cu/CuAl-MMO-400, (c2) Cu/CuAl-MMO-500 and (d2) Cu/CuAl-MMO-600, with size distribution shown in the inset. The corresponding HR-TEM lattice fringe images are shown in (a3), (b3), (c3) and (d3), respectively.

Table 1
Composition and structural properties of various samples.

Sample	BET Area ($m^2\ g^{-1}$)	Pore Volume ($cm^3\ g^{-1}$)	Pore Size (nm)	Cu Size[a] (nm)	Cu Size[b] (nm)	Surface Cu^0 Concentration[c] (mmol g^{-1})	Cu^0/Cu^{+}[d]
CuAl-MMO	53.7	0.33	24.4	–	–	–	–
Cu/CuAl-MMO-300	40.8	0.28	27.1	6.1	6.1	1.15	0.65
Cu/CuAl-MMO-400	48.7	0.27	22.6	6.8	6.7	1.12	0.85
Cu/CuAl-MMO-500	37.0	0.29	31.6	7.4	7.5	0.83	1.02
Cu/CuAl-MMO-600	31.9	0.18	22.9	8.5	8.2	0.72	1.18

[a] Cu Crystallite size was determined by XRD with the Scherrer equation.
[b] Mean Cu particle size was measured by TEM images.
[c] surface Cu^0 concentration was calculated based on the results of N_2O titration.
[d] Cu^0/Cu^+ molar ratio was determined by XAES.

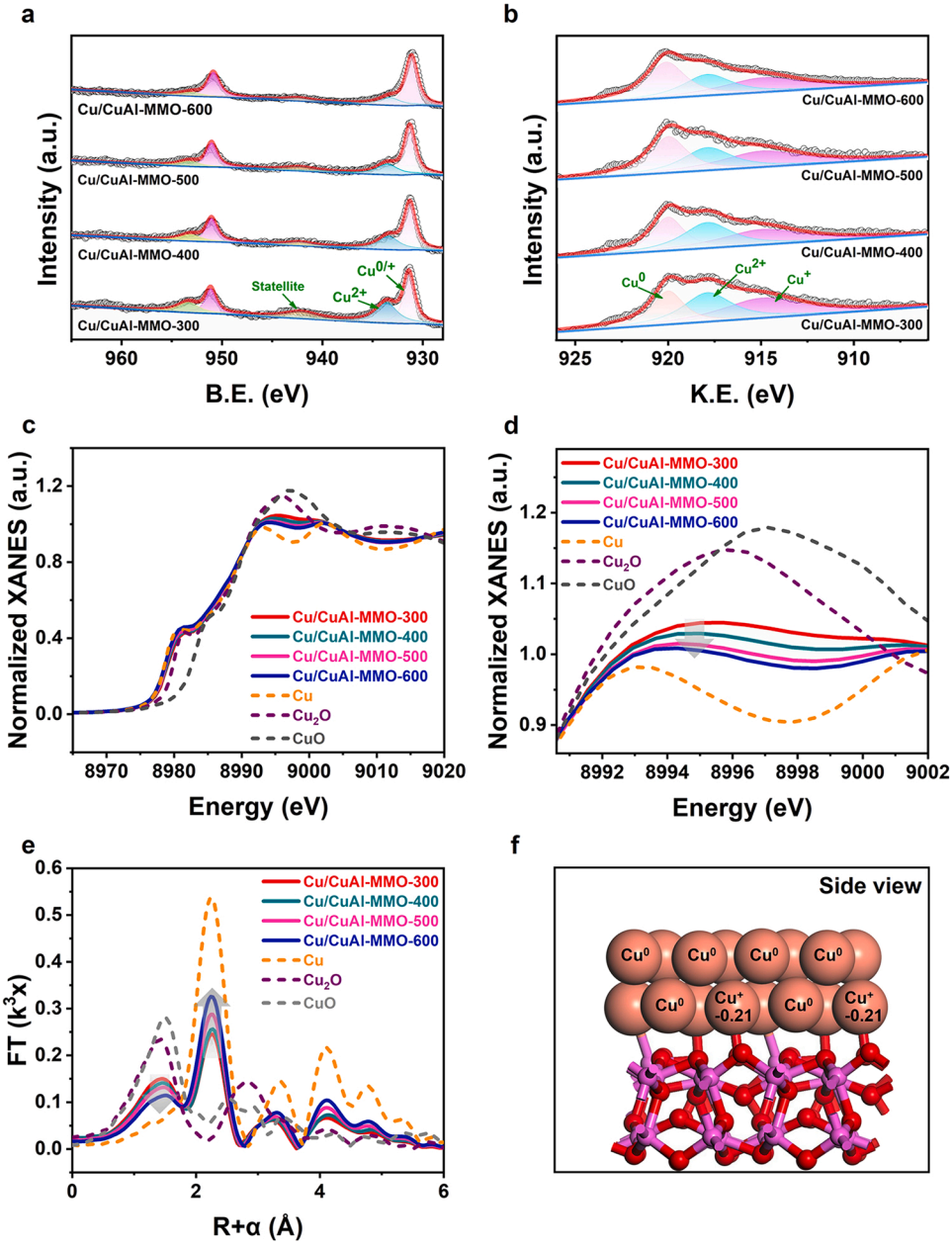

Fig. 3. (a) XPS spectra of Cu 2*p* and (b) corresponding XAES spectra of Cu LMM for Cu/CuAl-MMO-300, Cu/CuAl-MMO-400, Cu/CuAl-MMO-500, and Cu/CuAl-MMO-600, respectively. (c) Normalized intensity of Cu K-edge XANES spectra for Cu/CuAl-MMO-300, Cu/CuAl-MMO-400, Cu/CuAl-MMO-500 and Cu/CuAl-MMO-600, respectively. (d) Enlarged view of absorption edge selected from (c). (e) Corresponding Fourier transform k3-weighted EXAFS spectra in R space for Cu/CuAl-MMO-300, Cu/CuAl-MMO-400, Cu/CuAl-MMO-500 and Cu/CuAl-MMO-600, respectively. (f) Bader charge analysis of Cu/CuAl-MMO based on DFT calculations.

XAFS analysis was performed to demonstrate more specific structure of Cu species, and Cu K-edge XANES spectrum (Fig. 3c–d) from Cu/CuAl-MMO-300 to Cu/CuAl-MMO-600 display that the intensity of the white line gradually reduces in the comparison with Cu_2O, but the edge characteristics for monometallic Cu are obviously found [45]. This reveals that Cu^0 and Cu^+ co-exist, and Cu^0/Cu^+ ratio gradually enhances with the rise of reduction temperature. For these four Cu/CuAl-MMO samples, Fig. 3e shows the detailed atomic configuration in R space by

Fourier transform, and then the corresponding results of linear combination fitting (Fig. S8 and Table S2) are obtained by using a Cu foil (Cu^0) and a Cu_2O reference (Cu^+) [46]. The peaks at 1.89 and 2.54 Å according with the first shell of Cu_2O-like phase and the first shell of monometallic Cu, respectively. As the reduction temperature of these Cu/CuAl-MMO samples rises (Fig. 3e), the intensity of former peak decreases significantly; whilst the latter peak increases. Curve-fitting results (Table S2) disclose that the coordination number (CN) of Cu–O bond reduces from 1.6 (Cu/CuAl-MMO-300) to 1.0 (Cu/CuAl-MMO-400), to 0.6 (Cu/CuAl-MMO-500) and then to 0.1 (Cu/CuAl-MMO-600); while the CN of Cu–Cu bond correspondingly increases from 5.7 to 7.2, to 8.1 and then to 8.2. The decrease of Cu–O coordination and increase of Cu–Cu coordination further confirm the increase of the Cu^0/Cu^+ concentration, which is consistent with the results of XAES. Notably, by changing the reduction temperature in the structural topotactic transformation of LDHs precursor, the Cu^0/Cu^+ ratio of Cu/CuAl-MMO catalysts can be tuned. In addition, Bader charge analysis on Cu/CuAl-MMO sample (Fig. 3f) illustrates that Cu atoms at the interface transfers electrons (0.21 |e|) to O atoms in the support, leading to the formation of Cu^+ species.

3.2. Reaction evaluations toward catalytic transfer hydrogenation of furfural

For this study, FAL was employed to assess the catalytic behavior of CTH reaction over CuAl-MMO and four Cu/CuAl-MMO samples. According to the calculation, the carbon balance over these samples is above 95.8%. The FAL conversion and furfuryl alcohol (FOL) selectivity (200 °C, 0.1 MPa N_2) are shown in Fig. 4a and Table 2. With the increase of the sample reduction temperature, the FOL selectivity of all these samples approaches 100% at 1 h; while the catalytic activity first increases and then decreases, and the Cu/CuAl-MMO-400 catalyst shows the highest FAL conversion (98.0%). The reaction rates (Table 2) give the following sequence: Cu/CuAl-MMO-400 (0.125 mol_{FAL} g_{cat}^{-1} h^{-1}) > Cu/CuAl-MMO-300 (0.092 mol_{FAL} g_{cat}^{-1} h^{-1}) > Cu/CuAl-MMO-500 (0.076 mol_{FAL} g_{cat}^{-1} h^{-1}) > Cu/CuAl-MMO-600 (0.043 mol_{FAL} g_{cat}^{-1} h^{-1}). Notably, the Cu/CuAl-MMO-400 sample exhibits the highest catalytic activity (Fig. S9), which is at the highest level compared to non-noble metal catalysts ever reported (Table S3). In addition, we tested the catalytic performance of Al_2O_3 support, which was almost inert for CTH reaction of FAL (Fig. S9). We further evaluated the CTH reaction of other typical unsaturated aldehydes and hydrogen donors over CuAl-MMO-400. Similar performance was also obtained (Table S4), demonstrating the universality of CuAl-MMO-400 catalyst for CTH reaction.

Fig. 4b–c and Table S5–**S6** show the detailed investigations on reaction factors (reaction temperature and N_2 pressure) over Cu/CuAl-MMO-400 sample. When the reaction temperature rises from 180 °C to 200 °C, the FAL conversion rapidly increases from 52.9% to 98.0%, while the FOL selectivity slightly decreases from 99.2% to 97.9%. Then, from 200 °C to 240 °C, the conversion remains basically unchanged, but the FOL selectivity decreases rapidly with the formation of the by-product 2-methylfuran (2-MF). In Fig. 4c, the other products obtained under the condition of 1 MPa N_2 include decarbonization product (furan) and coupling products. In the case of N_2 pressure, the FAL conversion of 98.0% and the optimal FOL selectivity (97.9%) are obtained at 0.1 MPa. According to the evaluation consequence and principium of minimum energy consumption, N_2 pressure of 0.1 MPa and reaction temperature of 200 ℃ were selected as the optimum reaction conditions. In addition, the reusability of Cu/CuAl-MMO-400 was tested through five cycles under the same reaction conditions (Fig. 4d). The FOL selectivity still maintains > 96% and the FAL conversion drops slightly from 99% to 95% after five cycles. The structure and morphology characterizations (XRD, SEM, TEM and XPS) of the used catalyst display no significant change in comparison with the fresh one (Fig. S10 and S11). The results above demonstrate a satisfactory stability and recyclability of the Cu/CuAl-MMO-400 catalyst, originating from the advantages of its preparation method. In situ growth process of Cu nanoparticles from LDHs precursors induces a strong metal-support interaction, which would inhibit the agglomeration and sintering of metal nanoparticles [20,47]. Furthermore, the XAES characterizations (Fig. S11) of Cu/CuAl-MMO-400 catalyst before and after the reaction do not show obvious change in the Cu^0/Cu^+ ratio, indicating a good structural stability.

To build the structure-activity correlation of Cu/CuAl-MMO samples,

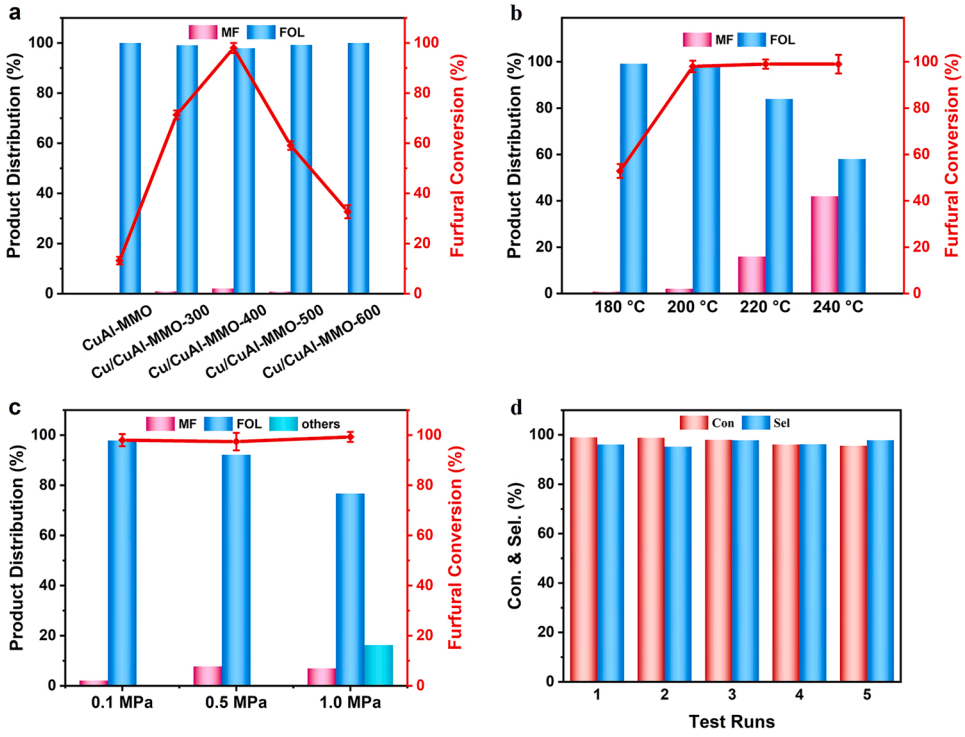

Fig. 4. (a) Catalytic performance of various samples toward CTH reaction of FAL: CuAl-MMO, Cu/CuAl-MMO-300, Cu/CuAl-MMO-400, Cu/CuAl-MMO-500, and Cu/CuAl-MMO-600. Catalytic conversion and corresponding product distribution as a function of (b) reaction temperature and (c) N_2 pressure for Cu/CuAl-MMO-400. (d) Reusability tests on Cu/CuAl-MMO-400 catalyst for five cycles. Reaction conditions: FAL (0.6 g), catalyst (0.05 g), 2-POL (18 mL), temperature (200 °C), time (1 h), N_2 pressure (0.1 MPa).

Table 2
Catalytic performances of various samples toward CTH reaction of FAL with 2-POL as the hydrogen source.

Sample[a]	Conversion (%)	Selectivity (%)	Hydrogen Balance[b] (%)	Carbon Balance[c] (%)	Reaction Rate ($mol_{FAL}\ g_{cat}^{-1}\ h^{-1}$)	TOF[d] (h^{-1})
CuAl-MMO	13.2	100.0	74.4	98.3	0.017	–
Cu/CuAl-MMO-300	71.3	99.1	83.8	96.9	0.092	31.8
Cu/CuAl-MMO-400	98.0	97.9	70.5	95.8	0.125	52.2
Cu/CuAl-MMO-500	59.1	99.2	83.5	96.5	0.076	46.9
Cu/CuAl-MMO-600	32.7	100.0	82.7	> 99.0	0.043	32.0

[a] Reaction conditions: 0.05 g of catalyst, 0.6 g of FAL, 18 mL of 2-POL, 0.1 MPa N_2, 200 °C, 1 h. Conversion and selectivity were determined by GC-MS.
[b] Hydrogen balance represents the transfer efficiency of hydrogen.
[c] Carbon balance represents the total selectivity of the liquid products.
[d] Turnover frequency (TOF, h^{-1}) is calculated as consumption rate of FAL per surface Cu atom.

reaction rate (Table 2) as a function of surface $Cu^+/(Cu^0+Cu^+)$ ratio were studied (illustrated in Fig. 5). From Cu/CuAl-MMO-300 to Cu/CuAl-MMO-600, the reaction rate exhibits a variation tendency of volcanic type *vs.* $Cu^+/(Cu^0+Cu^+)$ ratio, with the maximum reaction rate (0.125 $mol_{FAL}\ g_{cat}^{-1}\ h^{-1}$) obtained in Cu/CuAl-MMO-400 sample. This confirms that the surface Cu^0 and Cu^+ species serve as synergetic dual active sites toward the CTH reaction of FAL. Then, the turnover frequency (TOF) values are calculated based on both Cu^0 and Cu^+ species on catalyst surface, which give a following sequence (Table 2): Cu/CuAl-MMO-400 (52.2 h^{-1}) > Cu/CuAl-MMO-500 (46.9 h^{-1}) > Cu/CuAl-MMO-600 (32.0 h^{-1}) > Cu/CuAl-MMO-300 (31.8 h^{-1}). In addition, CO_2-TPD technique and IR spectroscopy of pyridine adsorption (Py-IR) were utilized to investigate the influence of acidity and basicity on catalytic performance [48]. As shown in Fig. S12, the profile of CuAl-MMO sample only shows a CO_2 desorption peak attributed to strong Lewis base site, which is absent in the reduced samples. In the Py-IR spectra (Fig. S13), all these samples display an obvious band at 1445 cm^{-1}, which is identified as the Lewis acid site of Cu^+. No significant difference can be observed, indicating similar acid-base properties of these four Cu/CuAl-MMO samples. However, their catalytic activities are rather different, suggesting that the surface acid-base properties are not the main factor affecting their catalytic performance.

3.3. Reaction mechanism on catalytic transfer hydrogenation of furfural

For the CTH reaction of FAL, three key stages are essential: (1) dehydrogenation of hydrogen donors, (2) hydrogenation of hydrogen acceptors, and (3) transfer of active hydrogen species between these two substrates. Since the dehydrogenation process on catalyst surface involves the cleavage of O−H and C−H bonds to obtain atomic H, *in situ* FT-IR spectra was utilized to study the adsorption of 2-POL on the surface of Cu/CuAl-MMO-400 (Fig. 6a). The pure 2-POL was directly blown into the reaction tank for 30 min at temperature of 25, 50, 100, 150 and 200 °C, and then He was injected for 15 min to eliminate the gaseous and physical adsorption of 2-POL for determination of chemical

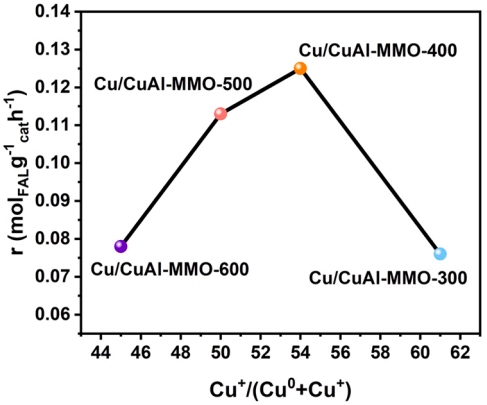

Fig. 5. Reaction rate as a function of $Cu^+/(Cu^0+Cu^+)$ ratio.

adsorption. As for the gas phase 2-POL, a strong band (1162 cm^{-1}) attributed to the ν(C−O) is observed at 25 °C. For the Cu/CuAl-MMO-400 sample (Fig. 6a), from 25 to 200 °C, the peak of ν(C−O) shows a successive red-shift from 1162 to 1147 cm^{-1}, and the other peaks have no obvious change, which is attributed to the adsorption of C−O bond in 2-POL over the Cu/CuAl-MMO-400 sample. However, *in-situ* FT-IR spectroscopy of 2-POL adsorption at 200 °C (Fig. S14) was performed on the Cu sample without Cu^+ species, and it was found that ν(C−O) only showed a red-shift of 7 cm^{-1}, indicating the more conducive for Cu^+ site of the Cu/CuAl-MMO-400 to the activation adsorption of 2-POL. To further reveal the active site and adsorption configuration of 2-POL, a comparative DFT study was carried out on Cu and Cu/CuAl-MMO-400 samples. In view of consequence from DFT-Grimme's D3 correction, on the surface of Cu sample (Fig. 6b), the O atom in C−O bond of 2-POL binds to the Cu^0 site, the O atom in C−O bond of 2-POL binds to the Cu^0 site (C−O bond length: 1.464 Å; adsorption energy: −0.48 eV). As for the Cu/CuAl-MMO sample (Fig. 6b), the O atom in C−O bond undergoes activation adsorption (C−O bond length: 1.471 Å) at interface Cu^+ site, with the adsorption energy of − 0.56 eV. The results above confirm that the C−O bond in 2-POL is more inclined to adsorb on the Cu^+ site.

Similar to the characterization technique of 2-POL, the adsorption of pure FAL on the surface of Cu/CuAl-MMO-400 was studied by *in-situ* FT-IR spectroscopy and DFT calculations. In the case of gas-phase FAL (Fig. 6c), a strong band at 1677 cm^{-1} attributed to ν(C═O) is found at 25 °C [5]. For the Cu/CuAl-MMO-400 sample (Fig. 6c), the peak of ν(C═O) shows a significant red-shift (10 cm^{-1}) from 25 to 200 °C accompanied with a decrease in relative intensity; and a new band appears at 1590 cm^{-1}, which is assigned to ν(C═C) in FAL. At a low temperature, FAL interacts with the catalyst weakly through a like η^2-(C, O)-aldehyde adsorption mode (weak adsorption of C═O and C═C). As the temperature rises to the reaction temperature (200 °C), the FAL is adsorbed in a η^1-(O) adsorption mode (strong adsorption of C═O) *via* the aldehyde group with a largely decreased intensity of C═O bond, and the free state of ν(C═C) simultaneously reappears. Notably, the adsorption peak of FAL on Cu catalyst (the control sample) at 200 °C (Fig. S15) shows almost no shift compared with the adsorption peak of gas phase at 25 °C, indicating that FAL is not easily adsorbed on Cu^0 site. DFT calculations show that for the Cu(111) system (Fig. S16 and Fig. 6d), the O atom in C═O bond of FAL is adsorbed at the Cu^0 site (tilted adsorption), with an adsorption energy of − 0.56 eV and C═O bond length of 1.242 Å. In the case of Cu/CuAl-MMO sample (Fig. S17), for the α-Cu site, furfural molecule is adsorbed at the surface α-Cu^0 (adsorption energy: −0.60 eV) instead of the interface α-Cu^+ due to the steric hindrance. In the case of β-Cu site, the adsorption energies of furfural molecule at the interface β-Cu^+ and the surface β-Cu^0 are − 0.88 eV and − 0.39 eV, respectively. Therefore, the most stable adsorption configuration of furfural (at the interface β-Cu^+ site) is chosen for the subsequent mechanism study. As shown in Fig. 6d, the O atom in C═O bond undergoes activation adsorption (C═O bond length: 1.255 Å) at the interface Cu^+ sites, with an adsorption energy of − 0.88 eV. The results verifies that C═O bond in FAL is more inclined to adsorb on the Cu^+ site. In addition, as a control catalytic reaction, the

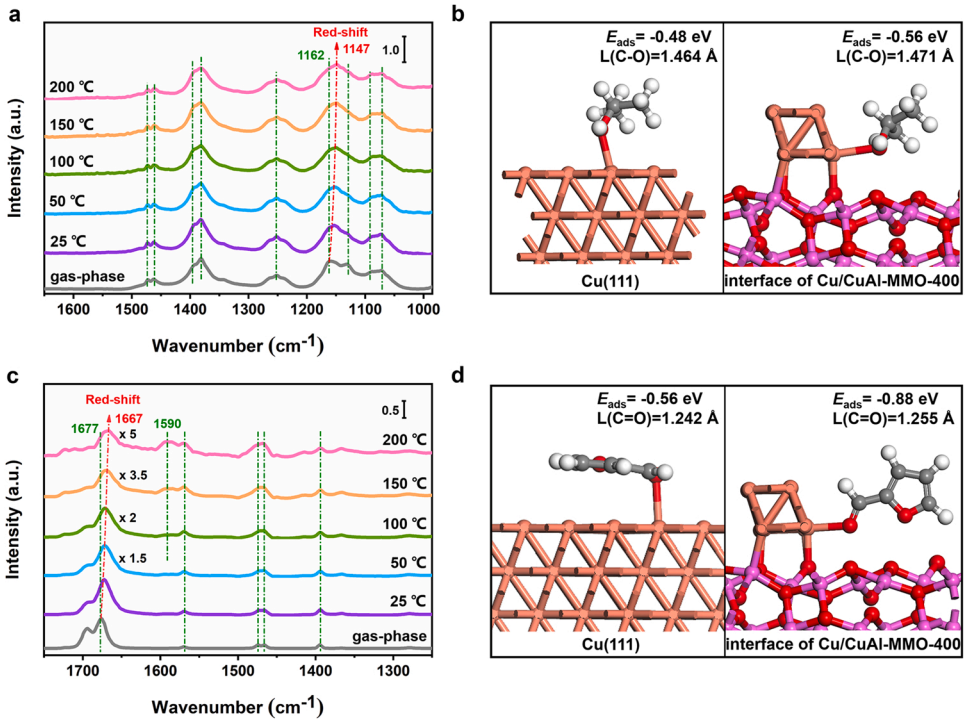

Fig. 6. (a) *In situ* FT-IR spectra of 2-POL adsorption at 25 °C on blank sample, and on Cu/CuAl-MMO-400 from 25 to 50, 100, 150 and 200 °C. (b) The optimal adsorption structure of 2-POL on the surface of Cu(111) and interface of Cu/CuAl-MMO-400. (c) *In situ* FT-IR spectra of FAL adsorption at 25 °C on blank sample, and on Cu/CuAl-MMO-400 from 25 to 50, 100, 150 and 200 °C. (d) The optimal adsorption structure of FAL on the surface of Cu (111) and interface of Cu/CuAl-MMO-400.

dehydrogenation reaction of 2-POL in the absence of FAL was studied (Fig. S18), and the Cu/CuAl-MMO-400 catalyst showed an excellent catalytic performance. The yield of acetone obtained in 2-POL dehydrogenation is significantly higher than that obtained in CTH reaction, indicating that FAL and 2-POL share the same active site in CTH reaction.

Based on the understanding of 2-POL or FAL adsorption on the Cu/CuAL-MMO-400, further exploration was made to study the adsorption of mixture (FAL and 2-POL) and possible reaction path in CTH reaction. Fig. 7a and Table S7 shows the relationship between the catalytic

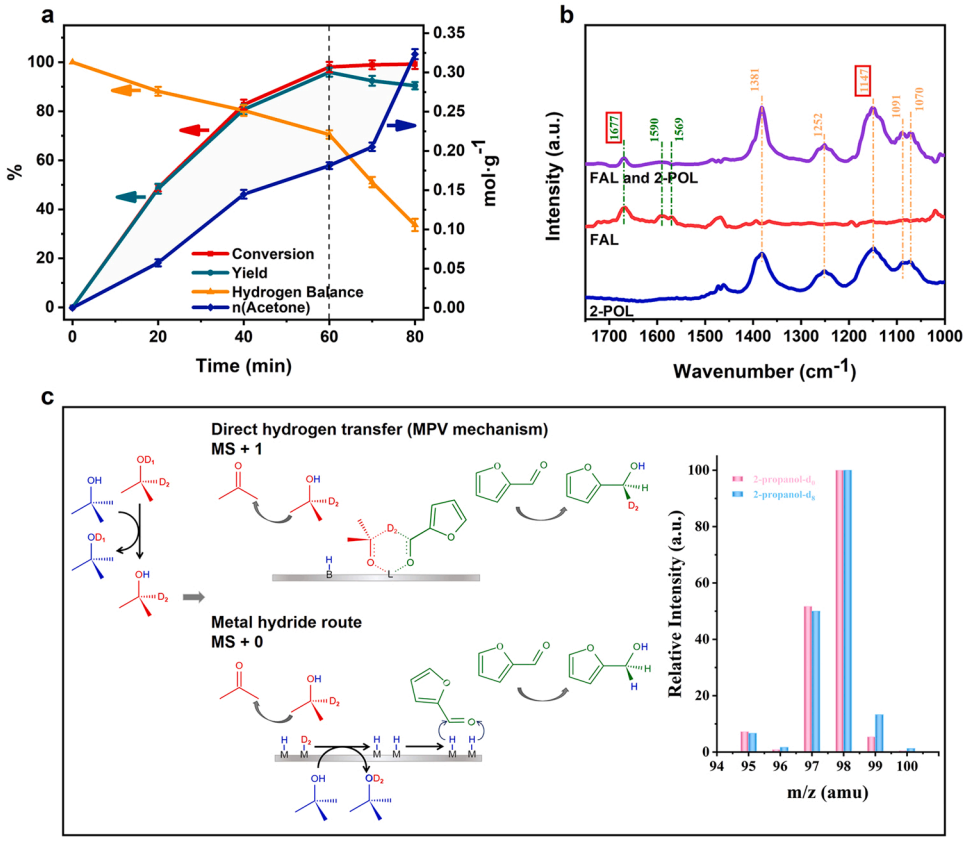

Fig. 7. (a) Catalytic performance (FAL conversion, FOL yield, hydrogen balance, acetone production) *vs.* reaction time for CTH reaction of FAL over Cu/CuAl-MMO-400. Reaction conditions: FAL (0.6 g), catalyst (0.05 g), 2-POL (18 mL), temperature (200 °C), time (1 h), N_2 pressure (0.1 MPa). (b) *In situ* FT-IR spectra of 2-POL adsorption, FAL adsorption, and mixture (FAL and 2-POL) adsorption at 200 °C on Cu/CuAl-MMO-400. (c) Schematic of the reaction mechanism *via* direct hydrogen transfer and metal hydride route, and the mass spectra of FOL obtained from FAL hydrogenolysis in *t*-butyl alcohol. Reaction conditions: FAL (0.6 g), catalyst (0.05 g), 2-POL-d_0 or 2-POL-d_8 (2 mL), t-butyl alcohol (16 mL), temperature (200 °C), N_2 pressure (0.1 MPa).

performance (FAL conversion, FOL yield, hydrogen balance and acetone production) and the reaction time on Cu/CuAL-MMO-400. As the reaction proceeds, the FAL conversion gradually increases whilst the FOL yield reaches to the maximum (96.0%) at 60 min, and then slightly decreases due to the formation of 2-MF. After FAL is completely converted to FOL, the hydrogen balance decreases rapidly; and when the reaction proceeds for more than 70 min, the output of acetone increases rapidly. This indicates that the desorption of FOL provides more active sites for 2-POL and thus accelerates the formation of acetone. Then, both FAL and 2-POL were simultaneously purged into the reactor at reaction temperature (200 °C) to conduct FT-IR measurements. The adsorption characteristic peaks of the mixture (Fig. 7b) show the same characteristic peaks of pristine FAL plus pristine 2-POL in the range 1700 − 1500 and 1500 − 1000 cm^{-1}, respectively, and no new band is observed. This confirms that the simultaneous introduction of FAL and 2-POL does not change their respective adsorption states on the catalyst.

As shown in Fig. 7c, two reaction mechanisms have been proposed in the CTH reaction, *e.g.*, the Meerwein Ponndorf Verley (MPV) mechanism and the metal hydride route [49,50]. The important difference between the above two paths is whether the β-H of 2-POL transfers to carbonyl C of FAL adsorbed on catalyst surface during the H transfer process [51]. To study the CTH reaction mechanism of FAL with 2-POL as the hydrogen source on the Cu-based catalyst, the detailed mass fragmentation analysis using isotopically labeled chemicals was performed. In the measurement, 2-POL perdeuterated(-d_8) was used as hydrogen source instead of 2-POL unlabeled(-d_0). Since 2-POL-d_8 is used as the solvent, the FOL products obtained by the two routes have the same amount of deuteration, *t*-butyl alcohol is chosen as solvent. The *t*-butyl alcohol has the following characteristics: (1) it lacks β-H and therefore cannot undergo dehydrogenation to provide H for the CTH reaction; and (2) H atom in OH group of *t*-butyl alcohol can exchange with the active D atoms on catalyst surface [48]. In addition, OH/OD can be quickly exchanged between alcohols [52], and *t*-butyl alcohol is greatly excessive compared to 2-POL-d_8, which is beneficial for *t*-butyl alcohol to exchange most of the OD group of 2-POL-d_8 to OH group. Therefore, 2-POL-d_7 ($CD_3CD(OH)CD_3$) is the main hydrogen source in the actual reaction. Taking into account the above factors, there is a D atom in the product FOL through the MPV route, which is obtained by directly transferring the β-D of 2-POL-d_7 to the carbonyl C through a six-membered ring intermediate. Thus, it is expected that the resulting FOL exhibits a 1 amu MS shift. In contrast, since *t*-butyl alcohol rapidly exchanges D adsorbed on the catalyst surface into H, the FOL obtained from the metal hydride route is expected without D atom (no mass shift). Fig. 7c shows the mass fragmentation pattern of FOL produced by the CTH of FAL using 2-POL-d_0 and 2-POL-d_8 as the hydrogen donor respectively. The pink bars are the mass fragmentation analysis obtained by 2-POL-d_0, which match well with the NIST database. However, compared with 2-POL-d_0, when using 2-POL-d_8 as the hydrogen source, the analysis results (blue bars) display no significant mass shift. The results indicate that on the Cu/CuAl-MMO-400 catalyst, the CTH of FAL with 2-POL as hydrogen source mainly occurs through the metal hydride route.

Furthermore, DFT calculations were performed to study the correlation between adsorption configuration and reaction pathway on interface of Cu/CuAl-MMO sample. Firstly, according to the characteristics of the most stable chair-like structure of the six-membered ring,

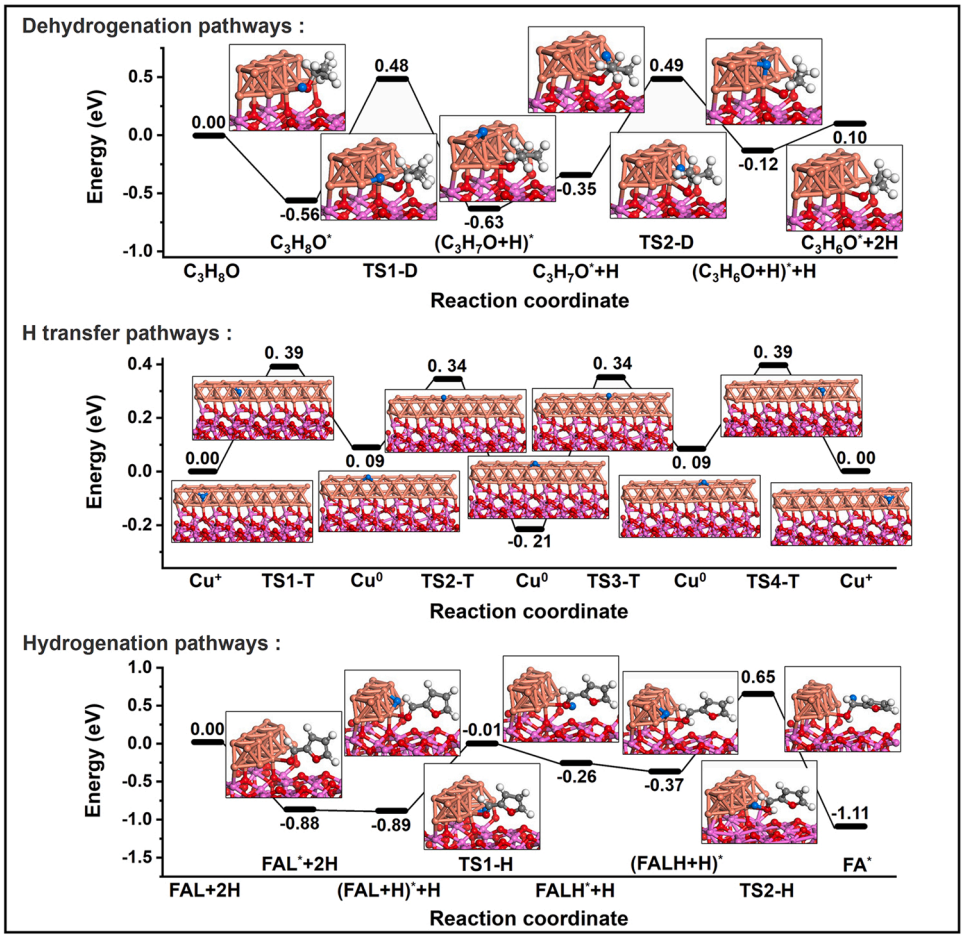

Fig. 8. Potential energies profile for the CTH reaction of FAL to FOL at the interface of Cu/CuAl-MMO-400 catalyst. Cu, orange; Al, pink; O, red; C, grey; H, white or blue.

the adsorption configuration of reactants in the MPV pathway was constructed. (Fig. S19) It was found that after optimization, FAL and 2-POL were adsorbed on the two Cu^+ sites, respectively, consistent with the experimental results. Then, we calculated the metal hydride path (Fig. 8 and **S15**) based on the three steps including 2-POL dehydrogenation, hydrogen transfer and FAL hydrogenation. For the dehydrogenation pathway, 2-POL adsorbs on Cu^+ site with an adsorption energy (−0.56 eV). The O−H bond of the adsorbed 2-POL breaks with an energy barrier of 1.04 eV (TS1-D), and the active H atom transfers to two adjacent Cu^0 sites in a bridge structure. Subsequently, the β-C−H bond breaks with an energy barrier of 0.84 eV (TS2-D), and H atom transfers to the FCC site of Cu^+, followed by a further migration to two adjacent Cu^0 sites in a bridge configuration with an energy barrier of 0.39 eV (TS1-T). As shown in Fig. S20, the cleavage of O−H bond in 2-POL in the dehydrogenation process is the rate-determining step, with a free energy barrier of 1.29 eV and an exothermic value of 0.17 eV. Then, H atom transfers on adjacent Cu^0 sites in a bridge configuration, with energy barriers of 0.25 eV (TS2-T) and 0.55 eV (TS3-T), respectively. Finally, the H atom adsorbed on the two Cu^0 sites in the bridge configuration transfers to the FCC site of Cu^+, with a reaction energy barrier of 0.30 eV (TS4-T). The results show that the hydrogen transfer energy barriers between Cu^+ and Cu^0 are very low, and the Cu^0 site facilitates the transfer of H atoms on the surface of the catalyst. In the final hydrogenation pathway, FAL undergoes activation adsorption on Cu^+ site (adsorption energy: −0.88 eV), followed by two successive hydrogenation processes at the O atom and C atom in the C═O bond, with corresponding reaction energy barriers of 0.88 eV and 1.02 eV. The desorption energy of FOL (1.11 eV) from Cu/CuAl-MMO-400 catalyst is relatively lower (Fig. 8) than that of previously reported work [53], indicating a facile desorption of the final product. The hydrogenation of C atom in C═O group of FAL is the rate-determining step, with a free energy barrier of 1.33 eV and an exothermic value of 1.08 eV (Fig. S20). Therefore, this whole CTH reaction is under a thermodynamic control. Therefore, the CTH reaction of FAL takes place through the metal hydride route with the synergistic effect of Cu^0 and Cu^+ of the Cu/CuAl-MMO catalyst. Furthermore, the structure of Cu strip in Cu/CuAl-MMO remains unchanged during the reaction process (Fig. S21).

4. Conclusion

In summary, Cu/CuAl-MMO catalysts with tunable dual active sites of Cu^0 and Cu^+ were prepared *via* an *in situ* structural topotactic transformation of Cu_2Al-LDHs at different reduction temperatures (300 −600 °C). The Cu/CuAl-MMO-400 sample gives an extremely high reaction rate (0.125 mol g^{-1} h^{-1}) toward CTH of FAL to FOL, in comparison with the non-precious metal catalysts ever reported. A joint study based on XPS, XAFS, *in situ* FT-IR substantiates that both FAL and 2-POL undergo activation adsorption on Cu^+ active site of the Cu/CuAl-MMO-400 catalyst. Isotopic labelling MS and DFT calculations confirm that the CTH reaction of FAL occurs through the metal hydride pathway with the synergistic effect of Cu^0 and Cu^+, in which Cu^0 promotes the transfer of H atoms on the catalyst surface whilst Cu^+ serves as dehydrogenation and hydrogenation active center, accounting for the excellent catalytic performance. This work provides detailed information on the synergistic catalysis of dual active sites and an in-depth understanding of the CTH reaction mechanism, which would be helpful for the development of high-added value utilization of biomass resources.

CRediT authorship contribution statement

Yingyu Ren: Data curation, Formal analysis, Writing – original draft. **Yusen Yang:** Conceptualization, Writing – review & amp; editing. **Lifang Chen:** Investigation. **Lei Wang:** Methodology. **Yawen Shi:** Investigation. **Pan Yin:** Investigation. **Wenlong Wang:** Methodology. **Mingfei Shao:** Methodology. **Xin Zhang:** Investigation. **Min Wei:** Conceptualization, Writing – review & editing.

Declaration of Competing Interest

The authors declare no competing financial interest.

Acknowledgments

This work was supported by the National Natural Science Foundation of China (22172006 and 22102006), the National Key R&D Program of China (2021YFC2103501), and the Fundamental Research Funds for the Central Universities (XK1803–05 and PT2021–04). The authors are thankful for the support of the BSRF (Beijing Synchrotron Radiation Facility) during the XAFS measurements at the beamline of 1W1B and 1W2B.

Appendix A. Supporting information

Supplementary data associated with this article can be found in the online version at doi:10.1016/j.apcatb.2022.121515.

References

[1] C. Higman, S. Tam, Advances in coal gasification, hydrogenation, and gas treating for the production of chemicals and fuels, Chem. Rev. 114 (2014) 1673–1708.
[2] Z. Zhang, J. Song, B. Han, Catalytic transformation of lignocellulose into chemicals and fuel products in ionic liquids, Chem. Rev. 117 (2017) 6834–6880.
[3] S. Gazi, Valorization of wood biomass-lignin *via* selective bond scission: a minireview, Appl. Catal. B: Environ. 257 (2019), 117936.
[4] M. Zhao, K. Yuan, Y. Wang, G. Li, J. Guo, L. Gu, W. Hu, H. Zhao, Z. Tang, Metal-organic frameworks as selectivity regulators for hydrogenation reactions, Nature 539 (2016) 76–80.
[5] Y. Yang, L. Chen, Y. Chen, W. Liu, H. Feng, B. Wang, X. Zhang, M. Wei, The selective hydrogenation of furfural over intermetallic compounds with outstanding catalytic performance, Green. Chem. 21 (2019) 5352–5362.
[6] C. Li, X. Zhao, A. Wang, G.W. Huber, T. Zhang, Catalytic transformation of lignin for the production of chemicals and fuels, Chem. Rev. 115 (2015) 11559–11624.
[7] J. Pang, J. Sun, M. Zheng, H. Li, Y. Wang, T. Zhang, Transition metal carbide catalysts for biomass conversion: a review, Appl. Catal. B: Environ. 254 (2019) 510–522.
[8] X. Li, P. Jia, T. Wang, Furfural: A promising platform compound for sustainable production of C4 and C5 chemicals, ACS Catal. 6 (2016) 7621–7640.
[9] S. Chen, R. Wojcieszak, F. Dumeignil, E. Marceau, S. Royer, How catalysts and experimental conditions determine the selective hydroconversion of furfural and 5–Hydroxymethylfurfural, Chem. Rev. 118 (2018) 11023–11117.
[10] Y. Deng, R. Gao, L. Lin, T. Liu, X.-D. Wen, S. Wang, D. Ma, Solvent tunes the selectivity of hydrogenation reaction over α-MoC catalyst, J. Am. Chem. Soc. 140 (2018) 14481–14489.
[11] D. Xu, R. Liu, J. Li, H. Zhao, J. Ma, Z. Dong, Atomically dispersed Co-N_4 sites anchored on N-doped carbon for aqueous phase transfer hydrogenation between nitroarenes and saturated N-heterocycles, Appl. Catal. B: Environ. 299 (2021), 120681.
[12] X. Lan, T. Wang, Highly selective catalysts for the hydrogenation of unsaturated aldehydes: a review, ACS Catal. 10 (2020) 2764–2790.
[13] S. Zhang, Z. Xia, M. Zhang, Y. Zou, H. Shen, J. Li, X. Chen, Y. Qu, Boosting selective hydrogenation through hydrogen spillover on supported-metal catalysts at room temperature, Appl. Catal. B: Environ. 297 (2021), 120418.
[14] L. Hu, J. Xu, S. Zhou, A. He, X. Tang, L. Lin, J. Xu, Y. Zhao, Catalytic advances in the production and application of biomass-derived 2,5-dihydroxymethylfuran, ACS Catal. 8 (2018) 2959–2980.
[15] V. Escande, C. Poullain, G. Clavé, E. Petit, N. Masquelez, P. Hesemann, C. Grison, Bio-based and environmental input for transfer hydrogenation using EcoNi(0) catalyst in isopropanol, Appl. Catal. B: Environ. 210 (2017) 495–503.
[16] Y. Chen, W. Liu, P. Yin, M. Ju, J. Wang, W. Yang, Y. Yang, C. Shen, Synergistic effect between Ni single atoms and acid–base sites: Mechanism investigation into catalytic transfer hydrogenation reaction, J. Catal. 393 (2021) 1–10.
[17] G.H. Wang, X. Deng, D. Gu, K. Chen, H. Tüysüz, B. Spliethoff, H.J. Bongard, C. Weidenthaler, W. Schmidt, F. Schüth, Co_3O_4 nanoparticles supported on mesoporous carbon for selective transfer hydrogenation of α,β-unsaturated aldehydes, Angew. Chem. Int. Ed. 55 (2016) 11101–11105.
[18] D. Wang, D. Astruc, The golden age of transfer hydrogenation, Chem. Rev. 115 (2015) 6621–6686.
[19] R.A. Farrar-Tobar, A. Dell'Acqua, S. Tin, J.G. de Vries, Metal-catalysed selective transfer hydrogenation of α,β-unsaturated carbonyl compounds to allylic alcohols, Green. Chem. 22 (2020) 3323–3357.
[20] Z. Gao, C. Li, G. Fan, L. Yang, F. Li, Nitrogen-doped carbon-decorated copper catalyst for highly efficient transfer hydrogenolysis of 5-hydroxymethylfurfural to

convertibly produce 2,5-dimethylfuran or 2,5-dimethyltetrahydrofuran, Appl. Catal. B: Environ. 226 (2018) 523–533.
[21] Z. Tang, H. Cao, Y. Tao, H.J. Heeres, P.P. Pescarmona, Transfer hydrogenation from glycerol over a Ni-Co/CeO_2 catalyst: a highly efficient and sustainable route to produce lactic acid, Appl. Catal. B: Environ. 263 (2020), 118273.
[22] H. Gómez Bernal, P. Benito, E. Rodríguez-Castellón, A.M. Raspolli Galletti, T. Funaioli, Synthesis of isopropyl levulinate from furfural: insights on a cascade production perspective, Appl. Catal. A Gen. 575 (2019) 111–119.
[23] R.A.W. Johnstone, A.H. Wilby, I.D. Entwistle, Heterogeneous catalytic transfer hydrogenation and its relation to other methods for reduction of organic compounds, Chem. Rev. 85 (1985) 129–170.
[24] M.S. Gyngazova, L. Grazia, A. Lolli, G. Innocenti, T. Tabanelli, M. Mella, S. Albonetti, F. Cavani, Mechanistic insights into the catalytic transfer hydrogenation of furfural with methanol and alkaline earth oxides, J. Catal. 372 (2019) 61–73.
[25] Q. Hu, G. Fan, L. Yang, X. Cao, P. Zhang, B. Wang, F. Li, A gas-phase coupling process for simultaneous production of γ-butyrolactone and furfuryl alcohol without external hydrogen over bifunctional base-metal heterogeneous catalysts, Green. Chem. 18 (2016) 2317–2322.
[26] W. Gong, C. Chen, Y. Zhang, H. Zhou, H. Wang, H. Zhang, Y. Zhang, G. Wang, H. Zhao, Efficient synthesis of furfuryl alcohol from H_2-hydrogenation/transfer hydrogenation of furfural using sulfonate group modified Cu catalyst, ACS Sustain. Chem. Eng. 5 (2017) 2172–2180.
[27] M. Zhang, Z. Li, Cu/Cu_2O-MC (MC=mesoporous carbon) for highly efficient hydrogenation of furfural to furfuryl alcohol under visible light, ACS Sustain. Chem. Eng. 7 (2019) 11485–11492.
[28] W. Fang, A. Riisager, Recent advances in heterogeneous catalytic transfer hydrogenation/hydrogenolysis for valorization of biomass-derived furanic compounds, Green. Chem. 23 (2021) 670–688.
[29] R. Zhang, J. Zhang, B. Zhao, L. He, A. Wang, B. Wang, Insight into the effects of Cu component and the promoter on the selectivity and activity for efficient removal of acetylene from ethylene on Cu-based catalyst, J. Phys. Chem. C. 121 (2017) 27936–27949.
[30] R. Zhang, J. Zhang, Z. Jiang, B. Wang, M. Fan, The cost-effective Cu-based catalysts for the efficient removal of acetylene from ethylene: the effects of Cu valence state, surface structure and surface alloying on the selectivity and activity, Chem. Eng. J. 351 (2018) 732–746.
[31] H. Yang, Y. Chen, X. Cui, G. Wang, Y. Cen, T. Deng, W. Yan, J. Gao, S. Zhu, U. Olsbye, J. Wang, W. Fan, A highly stable Copper-based catalyst for clarifying the catalytic roles of Cu^0 and Cu^+ species in methanol dehydrogenation, Angew. Chem. Int. Ed. 57 (2018) 1836–1840.
[32] E. Yuan, P. Ni, W. Zhuang, R. Jian, P. Jian, Synergic catalysis by a CuO-like phase and Cu^0 for anaerobic dehydrogenation of 2,3-butanediol, J. Catal. 382 (2020) 256–268.
[33] Z. Liu, F. Huang, M. Peng, Y. Chen, X. Cai, L. Wang, Z. Hu, X. Wen, N. Wang, D. Xiao, H. Jiang, H. Sun, H. Liu, D. Ma, Tuning the selectivity of catalytic nitriles hydrogenation by structure regulation in atomically dispersed Pd catalysts, Nat. Commun. 12 (2021) 1–8.
[34] J. Ma, Y. Chen, G. He, H. He, A robust H-transfer redox mechanism determines the high-efficiency catalytic performance of layered double hydroxides, Appl. Catal. B: Environ. 285 (2021), 119806.
[35] G. Kresse, J. Hafner, *Ab* initio molecular-dynamics simulation of the liquid-metal-amorphous-semiconductor transition in germanium, Phys. Rev. B. 49 (1994) 14251–14269.
[36] G. Kresse, D. Joubert, From ultrasoft pseudopotentials to the projector augmented-wave method, Phys. Rev. B Condens. Matter Mater. Phys. 59 (1999) 1758–1775.
[37] J.P. Perdew, K. Burke, M. Ernzerhof, Generalized gradient approximation made simple, Phys. Rev. Lett. 77 (1996) 3865–3868.
[38] S. Grimme, J. Antony, S. Ehrlich, H. Krieg, A consistent and accurate *ab* initio parametrization of density functional dispersion correction (DFT-D) for the 94 elements H-Pu, J. Chem. Phys. 132 (2010).
[39] G. Henkelman, B.P. Uberuaga, H. Jónsson, Climbing image nudged elastic band method for finding saddle points and minimum energy paths, J. Chem. Phys. 113 (2000) 9901–9904.
[40] G. Henkelman, H. Jónsson, A dimer method for finding saddle points on high dimensional potential surfaces using only first derivatives, J. Chem. Phys. 111 (1999) 7010–7022.
[41] W. Luo, W. Xie, M. Li, J. Zhang, A. Züttel, 3D hierarchical porous indium catalyst for highly efficient electroreduction of CO_2, J. Mater. Chem. A 7 (2019) 4505–4515.
[42] W. Gao, Y. Zhao, H. Chen, H. Chen, Y. Li, S. He, Y. Zhang, M. Wei, D.G. Evans, X. Duan, Core-shell Cu@(CuCo-alloy)/Al_2O_3 catalysts for the synthesis of higher alcohols from syngas, Green. Chem. 17 (2015) 1525–1534.
[43] K. Chen, J.L. Ling, C. De, Wu, In situ generation and stabilization of accessible Cu/Cu_2O heterojunctions inside organic frameworks for highly efficient catalysis, Angew. Chem. Int. Ed. 59 (2020) 1925–1931.
[44] X. Chang, A.F. Liu, B. Cai, J.Y. Luo, H. Pan, Y.B. Huang, Catalytic transfer hydrogenation of furfural to 2-methylfuran and 2-methyltetrahydrofuran over bimetallic Copper–Palladium catalysts, ChemSusChem 9 (2016) 3330–3337.
[45] I. Ro, Y. Liu, M.R. Ball, D.H.K. Jackson, J.P. Chada, C. Sener, T.F. Kuech, R. J. Madon, G.W. Huber, J.A. Dumesic, Role of the Cu-ZrO_2 interfacial sites for conversion of ethanol to ethyl acetate and synthesis of methanol from CO_2 and H_2, ACS Catal. 6 (2016) 7040–7050.
[46] M. Liu, L. Yuan, G. Fan, L. Zheng, L. Yang, F. Li, NiCu nanoparticles for catalytic hydrogenation of biomass-derived carbonyl compounds, ACS Appl. Nano Mater. 3 (2020) 9226–9237.
[47] M. Xu, S. He, H. Chen, G. Cui, L. Zheng, B. Wang, M. Wei, TiO_{2-x}-Modified Ni Nanocatalyst with Tunable Metal-Support Interaction for Water-Gas Shift Reaction, ACS Catal. 7 (2017) 7600–7609.
[48] G.S. Foo, D. Wei, D.S. Sholl, C. Sievers, Role of lewis and brønsted acid sites in the dehydration of glycerol over niobia, ACS Catal. 4 (2014) 3180–3192.
[49] T.C. Johnson, D.J. Morris, M. Wills, Hydrogen generation from formic acid and alcohols using homogeneous catalysts, Chem. Soc. Rev. 39 (2010) 81–88.
[50] J.S.M. Samec, J.E. Bäckvall, P.G. Andersson, P. Brandt, Mechanistic aspects of transition metal-catalyzed hydrogen transfer reactions, Chem. Soc. Rev. 35 (2006) 237–248.
[51] M.J. Gilkey, P. Panagiotopoulou, A.V. Mironenko, G.R. Jenness, D.G. Vlachos, B. Xu, Mechanistic insights into metal lewis acid-mediated catalytic transfer hydrogenation of furfural to 2–methylfuran, ACS Catal. 5 (2015) 3988–3994.
[52] S.F. Bureiko, G.S. Denisov, Spectroscopic study of hydrogen exchange processes and structure of intermediate complexes with intermolecular hydrogen bonds, J. Mol. Struct. 700 (2004) 49–53.
[53] S. Thongratkaew, C. Luadthong, S. Kiatphuengporn, P. Khemthong, P. Hirunsit, K. Faungnawakij, Cu-Al spinel-oxide catalysts for selective hydrogenation of furfural to furfuryl alcohol, Catal. Today 367 (2021) 177–188.